

# Photovoltaic Properties of Two-Dimensional (CH<sub>3</sub>NH<sub>3</sub>)<sub>2</sub>Pb(SCN)<sub>2</sub>I<sub>2</sub> Perovskite: A Combined Experimental and Density-Functional Theory Study

Zewen Xiao,<sup>1</sup> Weiwei Meng,<sup>1,2</sup> Bayrammurad Saparov,<sup>3,4</sup> Hsin-Sheng Duan,<sup>3,4</sup> Changlei Wang,<sup>1,2</sup>  
Chunbao Feng,<sup>1</sup> Weiqiang Liao,<sup>1</sup> Dewei Zhao,<sup>1</sup> Jianbo Wang,<sup>2</sup> David B. Mitzi,<sup>\*,3,4</sup> and Yanfa  
Yan<sup>\*,1</sup>

<sup>1</sup>*Department of Physics and Astronomy, and Wright Center for Photovoltaic Innovation and  
Commercialization, The University of Toledo, Toledo, Ohio 43606, USA*

<sup>2</sup>*School of Physics and Technology, Center for Electron Microscopy, MOE Key Laboratory of  
Artificial Micro- and Nano-structures, and Institute for Advanced Studies, Wuhan University,  
Wuhan 430072, China*

<sup>3</sup>*Department of Mechanical Engineering and Materials Science, Duke University, Durham,  
North Carolina 27708, USA*

<sup>4</sup>*Department of Chemistry, Duke University, Durham, North Carolina 27708, USA*

## AUTHOR INFORMATION

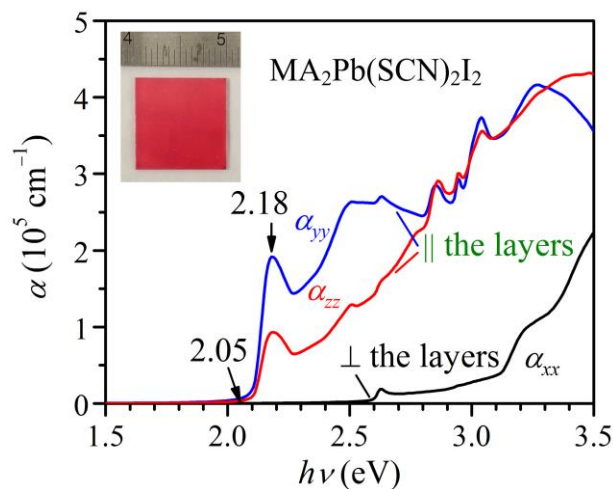
### Corresponding Authors

\* david.mitzi@duke.edu;

yanfa.yan@utoledo.edu

**ABSTRACT:** We explore the photovoltaic-relevant properties of the two-dimensional (2D)  $\text{MA}_2\text{Pb}(\text{SCN})_2\text{I}_2$  (where  $\text{MA} = \text{CH}_3\text{NH}_3^+$ ) perovskite using a combination of materials synthesis, characterization and density-functional theory calculation. We show that the electronic properties of  $\text{MA}_2\text{Pb}(\text{SCN})_2\text{I}_2$  are significantly different from those previously reported in literature. The layered perovskite with mixed-anions exhibits an indirect bandgap of about 2.04 eV, with a slightly larger direct bandgap of about 2.11 eV, in contrast to the previously reported bandgap of 1.57 eV. The carriers (both electrons and holes) are also found to be confined within the 2D layers. Our results suggest that the 2D  $\text{MA}_2\text{Pb}(\text{SCN})_2\text{I}_2$  perovskite may not be among the most promising absorbers for efficient single-junction solar cell applications. However, use as an absorber for the top cell of a tandem solar cell may still be a possibility, if films are grown with the 2D layers aligned perpendicular to the substrates.

## TOC GRAPHICS



**KEYWORDS:** Hybrid material, halide semiconductor, mixed-anion perovskite, optical properties, bandgap, carrier confinement

Organic-inorganic lead halide perovskite absorbers have attracted extensive attention due their excellent photovoltaic properties, such as suitable bandgap, high optical absorption, and long carrier lifetime.<sup>1-3</sup> Solar cells based on polycrystalline perovskite thin films have realized a record power conversion efficiency (PCE) of 20.1%. Despite the high record PCE, lead halide perovskite devices face a significant challenge—they are sensitive to moisture. The absorbers are known to react with moisture quickly and degrade to  $\text{PbI}_2$ , losing the excellent photovoltaic properties.<sup>4,5</sup> Efforts have been reported to mitigate moisture-induced degradation of perovskite solar cells. For example, encapsulation using glass plates and use of a carbon nanotube embedded polymer matrix (PMMA) were tested.<sup>6,7</sup> Hydrophobic cations such as phenylethylammonium (PEA) and alkyl ammonium as well as hydrophobic electrodes have also been used to improve the resistivity to moisture.<sup>8-10</sup>

Recently, it has been reported that adding pseudohalide  $\text{SCN}^-$  can improve both the cell efficiency and the moisture resistance of the perovskite absorbers.<sup>11,12</sup> The absorbers were reported to have compositions of  $\text{CH}_3\text{NH}_3\text{Pb}(\text{SCN})_2\text{I}$  ( $\text{MAPb}(\text{SCN})_2\text{I}$ ) or  $\text{MAPbI}_{3-x}(\text{SCN})_x$ , but were found to exhibit a bandgap similar to that of the  $\text{MAPbI}_3$  perovskite. The perovskite films were synthesized by introducing  $\text{Pb}(\text{SCN})_2$  into the perovskite precursor (for one-step process) or into the  $\text{PbI}_2$  precursor (for two-step process). However, an investigation<sup>13</sup> on single crystals grown using the same conditions as those reported for “ $\text{CH}_3\text{NH}_3\text{Pb}(\text{SCN})_2\text{I}$ ”<sup>11</sup> suggested that the compound is actually a two-dimensional (2D)  $\text{MA}_2\text{Pb}(\text{SCN})_2\text{I}_2$  perovskite. For  $\text{MA}_2\text{Pb}(\text{SCN})_2\text{I}_2$ , diffuse reflectance measurements gave a bandgap of  $\sim 1.57$  eV. Following this report, using density-functional theory (DFT) calculation, Ganose *et al.*<sup>14</sup> provided a possible explanation for the unusually small bandgap of  $\text{MA}_2\text{Pb}(\text{SCN})_2\text{I}_2$ , and further indicated that this 2D perovskite

exhibits a three-dimensional (3D) carrier mobility comparable to that of the parent 3D MAPbI<sub>3</sub> perovskite. So far, both experimental and DFT studies have indicated that the 2D MA<sub>2</sub>Pb(SCN)<sub>2</sub>I<sub>2</sub> perovskite may exhibit suitable properties for efficient single-junction solar cell application, including suitable bandgap and 3D mobile carriers, somewhat in contradiction to conventional wisdom for 2D materials—i.e., that a 2D material should exhibit a wider bandgap and lower carrier mobility along the direction perpendicular to the layers as compared to its 3D counterpart.<sup>8,15,16</sup> In this paper, we perform a comprehensive study of the photovoltaic properties of the 2D MA<sub>2</sub>Pb(SCN)<sub>2</sub>I<sub>2</sub> perovskite using a combination of materials synthesis, characterization and DFT calculation. We show that the 2D MA<sub>2</sub>Pb(SCN)<sub>2</sub>I<sub>2</sub> perovskite has a bandgap of slightly over 2.0 eV, much larger than the 1.57 eV value previously reported in the literature. We further find that the carriers (both electrons and holes) are confined within the 2D layers. The effective masses are nearly infinity along the direction perpendicular to the 2D layers. We therefore conclude that the 2D MA<sub>2</sub>Pb(SCN)<sub>2</sub>I<sub>2</sub> perovskite is not as promising a candidate as previously thought for efficient single-junction solar cell applications.

To determine the bandgap of MA<sub>2</sub>Pb(SCN)<sub>2</sub>I<sub>2</sub>, we synthesized MA<sub>2</sub>Pb(SCN)<sub>2</sub>I<sub>2</sub> both in powder and thin film forms. The measured X-ray diffraction (XRD) patterns of the MA<sub>2</sub>Pb(SCN)<sub>2</sub>I<sub>2</sub> powder and thin film are shown in Figures 1a and 1b, respectively. For comparison, we also calculated the XRD pattern of MA<sub>2</sub>Pb(SCN)<sub>2</sub>I<sub>2</sub>, as shown in Figure 1c, using the structure reported by Daub *et al.*<sup>13</sup> All diffraction peaks of both the powder and thin film samples are attributed to the MA<sub>2</sub>Pb(SCN)<sub>2</sub>I<sub>2</sub> phase, indicating that single-phase MA<sub>2</sub>Pb(SCN)<sub>2</sub>I<sub>2</sub> was formed in both the powder and thin film samples. The relative intensities of the *h*00 diffraction peaks with respect to the non *h*00 peaks are stronger for the thin film sample than for the powder sample, indicating that the thin film was highly oriented, with the *a*-axis

perpendicular to the substrate, as is typical for 2D layered materials.<sup>17,18</sup> It is noted that the XRD pattern of MA<sub>2</sub>Pb(SCN)<sub>2</sub>I<sub>2</sub> is different from that of the “MAPb(SCN)<sub>2</sub>I” thin film reported by Jiang *et al.*<sup>11</sup> (see Figure S1 in the Supporting Information). Therefore, the material reported by Jiang *et al.* should not be considered as single-phase MA<sub>2</sub>Pb(SCN)<sub>2</sub>I<sub>2</sub>. The colors of the single-phase MA<sub>2</sub>Pb(SCN)<sub>2</sub>I<sub>2</sub> powders and thin films are dark red and red (see Figure S2), respectively, consistent with the dark red color of single-crystal MA<sub>2</sub>Pb(SCN)<sub>2</sub>I<sub>2</sub>,<sup>13</sup> but in contrast to the black color reported for “MAPb(SCN)<sub>2</sub>I”.<sup>11</sup>

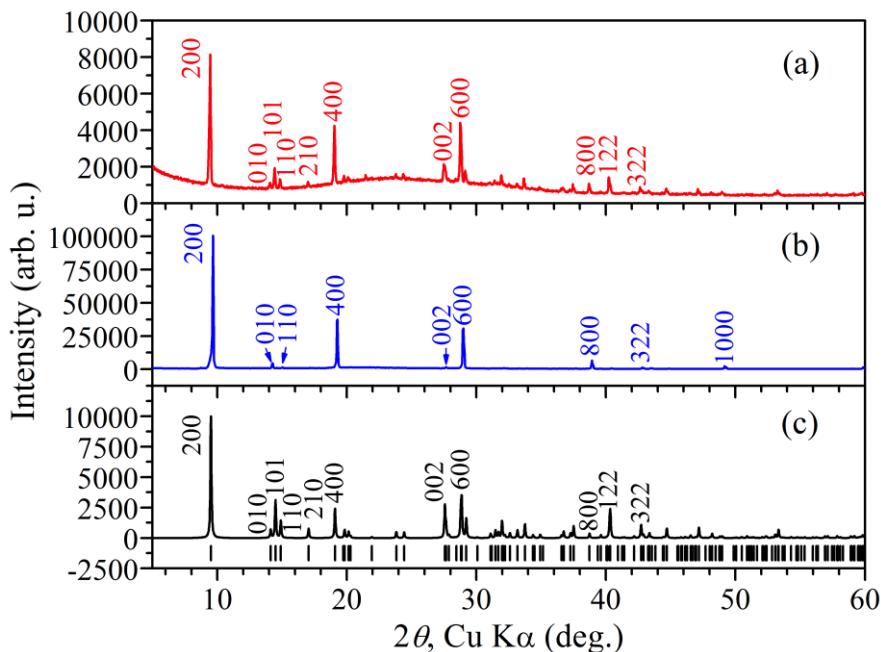


**Figure 1.** XRD patterns (Cu K $\alpha$  radiation) of MA<sub>2</sub>Pb(SCN)<sub>2</sub>I<sub>2</sub> (a) powders and (b) thin film. (c) Calculated XRD pattern of MA<sub>2</sub>Pb(SCN)<sub>2</sub>I<sub>2</sub>. The vertical bars indicate the calculated positions of diffraction peaks for MA<sub>2</sub>Pb(SCN)<sub>2</sub>I<sub>2</sub>.

Figure 2a shows the absorbance ( $A$ ) spectrum of a MA<sub>2</sub>Pb(SCN)<sub>2</sub>I<sub>2</sub> thin film, exhibiting a sharp absorption edge at 2.08 eV. Interestingly, this spectrum shows a sharp absorption peak at

2.25 eV, which is right above the bandgap. Similar sharp absorption peaks have also been observed in other typical 2D layered semiconductors such as  $LnCuOCh$  ( $Ln$  = lanthanide;  $Ch$  = chalcogen),<sup>19,20</sup>  $MS_2$  ( $M$  = Mo, W),<sup>21,22</sup>  $PbI_2$ ,<sup>23</sup> and  $(PEA)_2(MA)_2[Pb_3I_{10}]^8$  and are explained by the quantum confinement of the charge carriers. Figures 2b and 2c show the Tauc plots corresponding to the direct and indirect bandgap fits, respectively. From these Tauc plots, a direct bandgap of 2.11 eV and an indirect bandgap of 2.04 eV are obtained. These bandgaps are consistent with the red color of the  $MA_2Pb(SCN)_2I_2$  thin film, but much larger than the bandgap of 1.57 eV determined from the diffuse reflectance ( $R_\infty$ ) spectrum by Daub *et al.* (see Figure S3).<sup>13</sup> To further understand this discrepancy, we also measured the  $R_\infty$  spectrum of a  $MA_2Pb(SCN)_2I_2$  powder sample, prepared in a  $N_2$  filled glove box (Figure 2d). Our  $R_\infty$  spectrum reveals a similar feature as the one reported by Daub *et al.*<sup>13</sup>—i.e., an absorption edge appears at 790 nm (1.57 eV). However, the  $R_\infty$  spectrum also shows other features in the energy regions higher than 1.57 eV.

To understand more about the absorption features of the powder sample, the  $R_\infty$  spectrum is converted into Tauc plots. Figures 2e and 2f show the Tauc plots of the  $R_\infty$  spectrum corresponding to the direct and indirect bandgap fits, respectively. These Tauc plots show a distinct absorption peak at 2.08 eV, which is similar to the absorption peak at 2.25 eV seen in the Tauc plots measured from the  $MA_2Pb(SCN)_2I_2$  thin film. They strongly suggest a direct bandgap of 1.98 eV and/or an indirect bandgap of around 1.97 eV, slightly smaller than those obtained for the thin film. The Tauc plots also show additional absorption shoulders below the bandgaps, with extrapolated onsets of 1.52 eV (direct) and 1.51 eV (indirect). However, we believe that these features are not the real fundamental bandgaps of  $MA_2Pb(SCN)_2I_2$  due to two reasons: (1) the absorbance of these shoulders is much lower compared to the absorption above the proposed

bandgaps of 1.98 (direct fit) and 1.97 eV (indirect fit), which gives rise to the dark red coloration of the powder (vs. black); and (2) there was not a corresponding feature in the Tauc plot of the thin-film sample.

The origin of the absorption shoulder in the range of 1.5–2.0 eV seen in the  $R_\infty$  spectrum for the powder sample is not clear, but it is likely due to defects and/or impurity phases such as MAPbI<sub>3</sub> formed in the surface regions of the particles, due to the solid state pellet formation and subsequent grinding process, coupled with the ease with which this compound decomposes. Similar absorption shoulders have also been observed in the  $R_\infty$  spectra of other powder samples and have been attributed to the effects of defects.<sup>24,25</sup> It is noted that the fluorescence spectrum reported by Daub *et al.*<sup>13</sup> showed a weak emission peak at about 635 nm (1.95 eV), a strong emission peak at 702 nm (1.77 eV), and a less strong emission peak at 760 nm (1.63 eV). In a defective powder sample, it is reasonable to assume that the weak peak at about 1.95 eV is related to the bandgap emission and the peaks at 1.77 and 1.63 eV are due to defect and/or impurity-related emissions. However, to fully understand the nature of the optical transitions in this compound, temperature-dependent and time-resolved photoluminescence measurements are required and these results will be published as a separate study. Nonetheless, the bandgap values of 2.11 eV (direct) or 2.04 eV (indirect), measured from our 2D MA<sub>2</sub>Pb(SCN)<sub>2</sub>I<sub>2</sub> thin films, are much larger than that of 3D MAPbI<sub>3</sub> (1.57 eV),<sup>26</sup> as might be expected from the lower-dimensional structure.

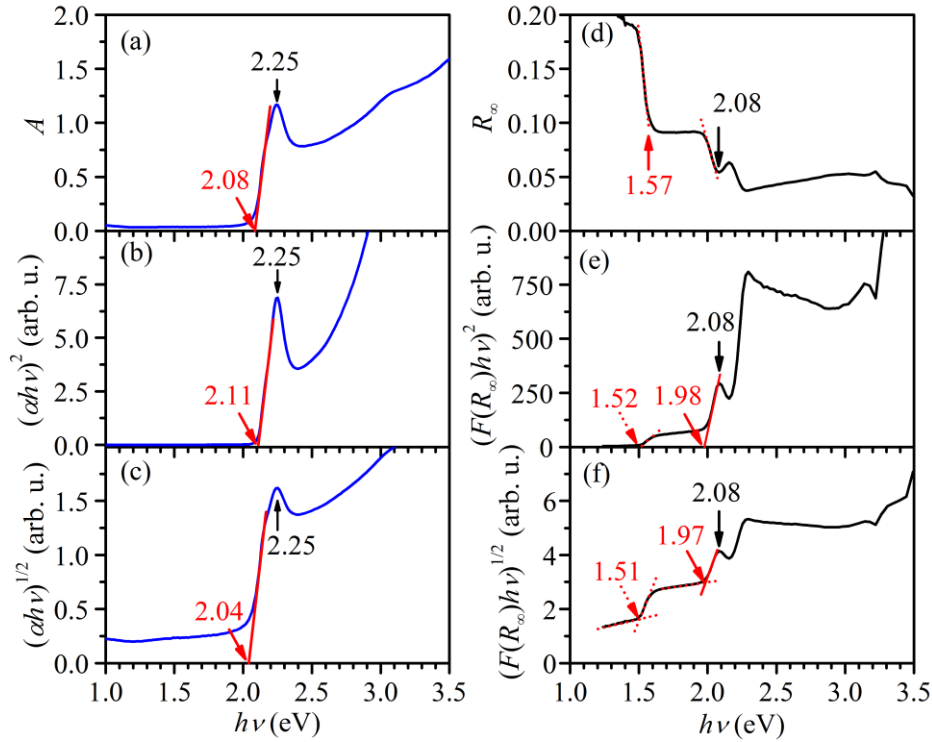


**Figure 2.** (a) Absorbance ( $A$ ) spectrum of a  $\text{MA}_2\text{Pb}(\text{SCN})_2\text{I}_2$  thin film. (b,c) Tauc plots of the  $A$  spectrum corresponding to (b) a direct and (c) an indirect optical bandgap of  $\text{MA}_2\text{Pb}(\text{SCN})_2\text{I}_2$ . (d) Diffuse reflectance ( $R_\infty$ ) spectrum of  $\text{MA}_2\text{Pb}(\text{SCN})_2\text{I}_2$  powders. (e,f) Tauc plots of the  $R_\infty$  spectrum corresponding to (e) a direct and (f) an indirect optical bandgap of  $\text{MA}_2\text{Pb}(\text{SCN})_2\text{I}_2$ .

We further employed DFT calculations to understand whether the 2D  $\text{MA}_2\text{Pb}(\text{SCN})_2\text{I}_2$  perovskite has a direct or indirect bandgap. Previous reports have shown that using the general gradient approximation (GGA) exchange-correlation with the Perdew–Burke–Ernzerhof (PBE)<sup>27</sup> functional, without considering the spin-orbit coupling (SOC) for Pb  $6p$  orbitals, can predict correctly the bandgap of the 3D  $\text{MAPbI}_3$  perovskite, due to the fact that the errors of using GGA and non-SOC cancel with each other when used concurrently.<sup>28</sup> When the SOC is considered, which is necessary for correctly interpreting the lower conduction band derived from Pb  $6p$

states,<sup>29</sup> the Heyd–Scuseria–Ernzerhof (HSE)<sup>30,31</sup> hybrid functional with a Hartree–Fock portion ( $\alpha$ ) of as large as 43% needs to be used to correctly predict the bandgap of the 3D MAPbI<sub>3</sub> perovskite.<sup>32,33</sup> We have repeated the band structure calculations of the 3D MAPbI<sub>3</sub> perovskite using the PBE non-SOC and HSE <sup>$\alpha=43\%$</sup> +SOC and obtained bandgaps of 1.57 eV and 1.50 eV, respectively. These bandgaps agree well with the experimentally measured bandgap of 1.57 eV. Therefore, we used the same PBE non-SOC and HSE <sup>$\alpha=43\%$</sup> +SOC methods to evaluate the electronic properties of the 2D MA<sub>2</sub>Pb(SCN)<sub>2</sub>I<sub>2</sub> perovskite. For self-consistency, we have used the calculated lattice constants for the electronic calculation (Table 1). The lattice constants calculated by the HSE <sup>$\alpha=43\%$</sup> +SOC method are closer to the experimental values<sup>13</sup> than those calculated using the PBE functional. The PBE non-SOC method predicts a direct bandgap of 2.11 eV and an indirect bandgap of 2.05 eV, whereas HSE <sup>$\alpha=43\%$</sup> +SOC method predicts a direct bandgap of 2.12 eV and an indirect bandgap of 2.06 eV. Both PBE non-SOC and HSE <sup>$\alpha=43\%$</sup> +SOC predict that the difference between the direct and indirect bandgap is as small as 0.06 eV for the 2D MA<sub>2</sub>Pb(SCN)<sub>2</sub>I<sub>2</sub> perovskite. These calculated bandgaps agree reasonably well with the experimental bandgaps, 2.11 eV (direct) and 2.04 eV (indirect), measured from the MA<sub>2</sub>Pb(SCN)<sub>2</sub>I<sub>2</sub> thin film. Therefore, based on our thin-film optical measurement and DFT calculations, we conclude that the 2D MA<sub>2</sub>Pb(SCN)<sub>2</sub>I<sub>2</sub> perovskite has an indirect (nearly direct) bandgap of about 2.04 eV, rather than 1.57 eV as previously reported in the literature.<sup>13,14</sup>

**Table 1.** Experimental and calculated lattice parameters and direct and indirect bandgaps ( $E_{g,dir}$  and  $E_{g,ind}$ , respectively) of  $MA_2Pb(SCN)_2I_2$ . The experimental lattice parameters are taken from Ref. 13. Percentage differences of calculated parameters from the experimental ones are shown in brackets.

Method	a (Å)	b (Å)	c (Å)	V (Å <sup>3</sup> )	$E_{g,dir}$ (eV)	$E_{g,ind}$ (eV)
Exp.	18.580(2) <sup>13</sup>	6.267(7) <sup>13</sup>	6.466(6) <sup>13</sup>	752.907 <sup>13</sup>	2.11	2.04
PBE non-SOC	18.909 (+1.77)	6.377 (+1.75)	6.631 (+2.56)	799.529 (+6.19)	2.11	2.05
HSE <sup><math>\alpha=43\%</math></sup> +SOC	18.841 (+1.40)	6.320 (+0.84)	6.530 (+0.99)	777.542 (+3.27)	2.12	2.06

Though both the PBE and HSE <sup>$\alpha=43\%$</sup> +SOC calculations correctly predict the band gaps of 2D  $MA_2Pb(SCN)_2I_2$  and 3D  $MAPbI_3$  perovskites, the latter interprets better the lower conduction band of these perovskites because it accounts for the SOC-induced splitting of the Pb 6*p* states. Therefore, we discuss the electronic structure of the 2D  $MA_2Pb(SCN)_2I_2$  perovskite based on the HSE <sup>$\alpha=43\%$</sup> +SOC calculation. It should be pointed out that for appropriate band structure calculations, the *k*-path should be carefully chosen so that paths representing *all* important directions for carrier transport are included. Figures 3a and 3b show the crystal structure of the orthorhombic 2D  $MA_2Pb(SCN)_2I_2$  perovskite and the corresponding first Brillouin zone, on which the labels of the high-symmetry *k*-points are taken from the Bilbao Crystallographic Server.<sup>34</sup> Figure 3c shows the calculated band structure along the *k*-path shown by the red line in

Figure 3b. It is seen that the valence band maximum (VBM) is located at the T point (0.0, 0.5, 0.5) (labeled as “U” in Ref. 14). The conduction band minimum (CBM) is slightly off the T point. Therefore, the 2D MA<sub>2</sub>Pb(SCN)<sub>2</sub>I<sub>2</sub> perovskite has a nearly direct bandgap. The difference between the direct and indirect bandgaps is about 0.06 eV. Figure 3d shows the calculated total and site-projected density of states. It is seen that the VBM consists mainly of I 5*p*/S 3*p*-Pb 6*s* antibonding states, while the CBM is dominated by Pb 6*p* states. The lower conduction band exhibits a clear SOC-induced splitting, as compared with that by PBE non-SOC (Figure S4). The orbital characteristics of the VBM and CBM also can be understood from the charge density maps of the VBM and CBM shown in Figures 4a and 4c, respectively. These results are generally consistent with those reported by Ganose *et al.*<sup>14</sup>

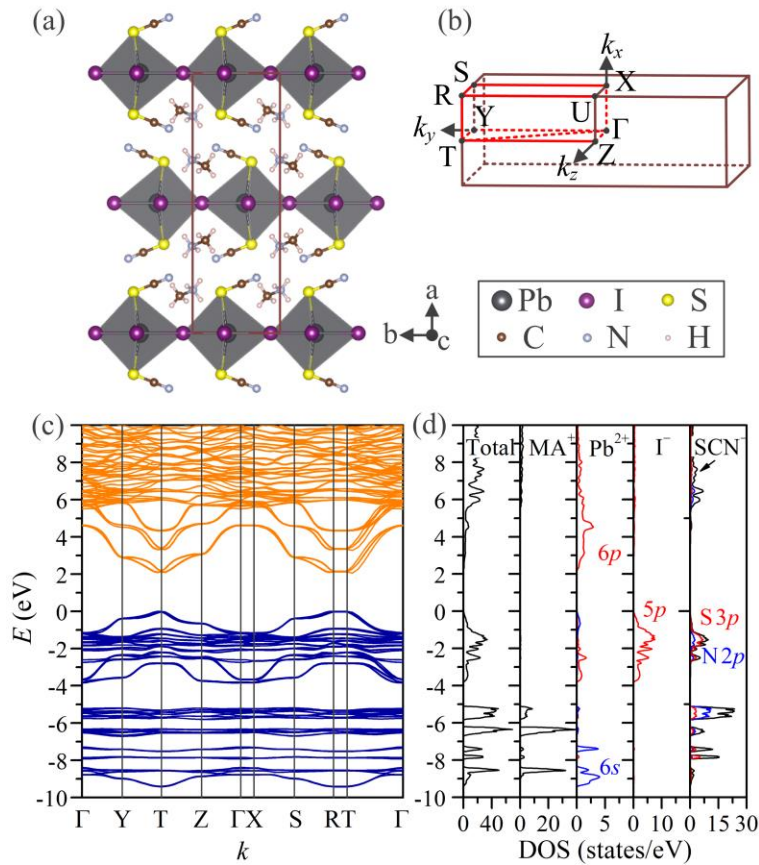


**Figure 3.** (a) Crystal structure of orthorhombic  $\text{MA}_2\text{Pb}(\text{SCN})_2\text{I}_2$  (space group  $Pnm2_1$ ) as viewed along the  $[001]$  directions. (b) The first Brillouin zone for the orthorhombic lattice of  $\text{MA}_2\text{Pb}(\text{SCN})_2\text{I}_2$  and the  $k$ -path (red line) used to plot the band structure in the present paper. (c) Band structure and (d) density of states of  $\text{MA}_2\text{Pb}(\text{SCN})_2\text{I}_2$  calculated with the  $\text{HSE}^{\alpha=43\%}+\text{SOC}$  method.

The calculated band structure shown in Figure 3c reveals dispersive characters for the lower conduction band and upper valence band for the 2D  $\text{MA}_2\text{Pb}(\text{SCN})_2\text{I}_2$  perovskite along the T–Z and T–Y directions, which are parallel to the layers. This dispersive feature can be understood by the strong I 5p S 3p–Pb 6s antibonding coupling, similar to the case of the 3D  $\text{MAPbI}_3$ .<sup>32</sup> The calculated effective masses for holes and electrons along the T–Z (i.e.,  $[010]$ ) direction are  $0.99 m_0$  and  $0.88 m_0$ , respectively, and those along the T–Y (i.e.,  $[001]$ ) direction are  $2.36 m_0$  and  $0.34 m_0$ , respectively. However, there is almost no dispersion for the states near the CBM and VBM along the T–R direction (i.e.,  $[100]$ ), which is attributed to the van der Waals interaction between the layers in the  $[100]$  direction. The calculated effective masses for both holes and electrons along the T–R direction are nearly infinity, indicating that the charge carriers are not mobile across the layers and are confined within the 2D layers. The charge carrier confinement is consistent with the calculated charge density maps of the VBM and CBM, shown in Figure 4. The VBM associated charge is mainly distributed in the  $[\text{PbI}_4\text{S}_2]$  octahedra layers, whereas and the CBM associated charge is in the Pb atomic planes. The confinement of electrons and holes are also clearly seen in the averaged charge density profiles shown in Figures 4b and 4d, respectively. Note that, Ganose *et al.*<sup>14</sup> did not include the states and the effective masses along the T–R direction (i.e. the “U”–R direction in this prior reference), leading to a conclusion

that the 2D MA<sub>2</sub>Pb(SCN)<sub>2</sub>I<sub>2</sub> perovskite has 3D carrier transport properties analogous to those in the 3D MAPbI<sub>3</sub> perovskite.

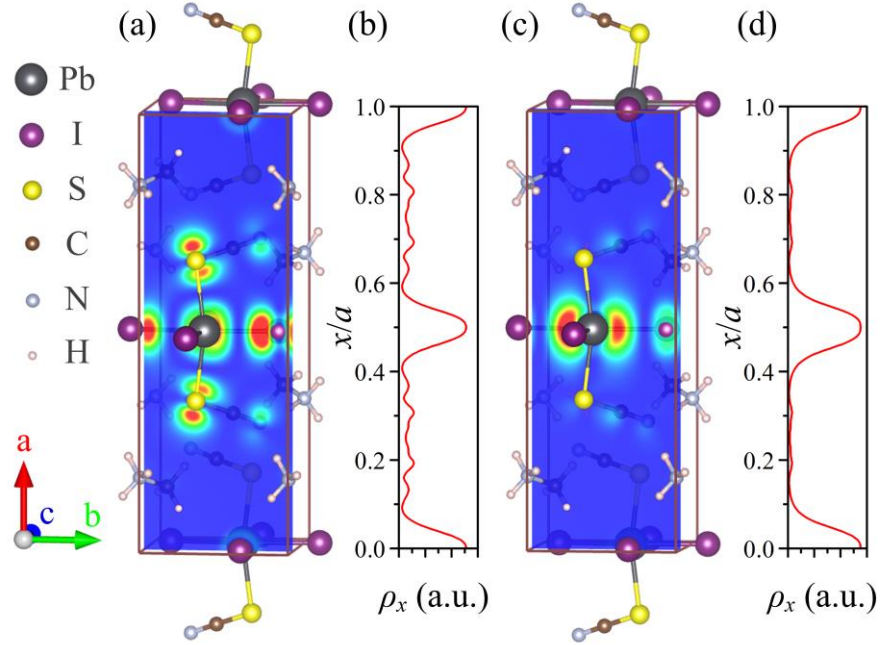


**Figure 4.** (a,c) VBM and CBM associated charge density maps within a slice perpendicular to the  $c$ -axis and passing through the Pb atom, and (b,d) averaged charge densities over the  $bc$  plane (perpendicular to the  $a$ -axis) ( $\rho_x$ ) for the 2D MA<sub>2</sub>Pb(SCN)<sub>2</sub>I<sub>2</sub> perovskite.

Finally, we discuss the optical properties of the 2D MA<sub>2</sub>Pb(SCN)<sub>2</sub>I<sub>2</sub> perovskite. Figure 5 shows the PBE calculated absorption coefficient for MA<sub>2</sub>Pb(SCN)<sub>2</sub>I<sub>2</sub>, exhibiting a strongly anisotropic character, due to the layered structure. The absorption contribution along the [100] direction crossing the layers ( $\alpha_{xx}$ ) is much weaker than that along the [010] and [001] directions parallel to the layers ( $\alpha_{yy}$ , and  $\alpha_{zz}$ , respectively). There is no noticeable absorption below 2.6 eV along the [100] direction. The absorptions along the [010] and [001] directions exhibit a peak at 2.18 eV, right above the absorption edge, consistent with the experimental optical spectra. The

absorption peak should be caused by the flat band along the T–R direction. Due to the  $p$ – $p$  transition feature, the 2D MA<sub>2</sub>Pb(SCN)<sub>2</sub>I<sub>2</sub> perovskite exhibits a high total absorption coefficient. Therefore, it may still be considered for use as the top cell of tandem solar cell applications, if films are grown with the 2D layers aligned perpendicular to the substrates, similar to the 1D Sb<sub>2</sub>Se<sub>3</sub> photovoltaics reported by Zhou et al.<sup>35</sup>, and if defect properties in MA<sub>2</sub>Pb(SCN)<sub>2</sub>I<sub>2</sub> prove to be benign.

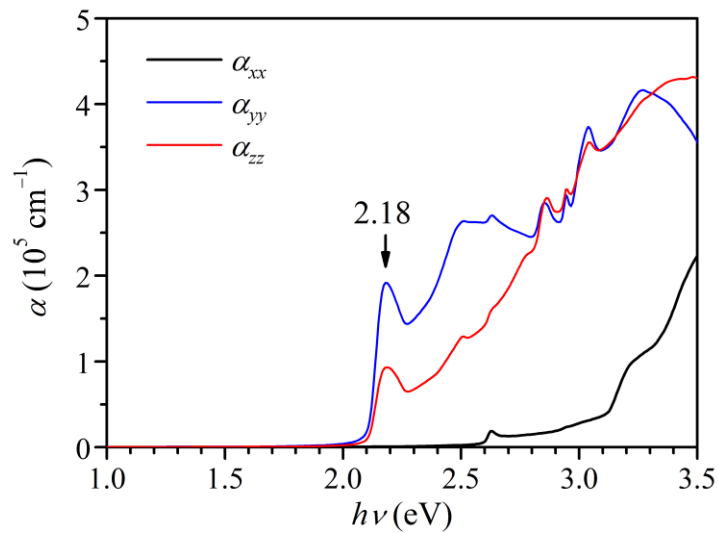


**Figure 5.** Calculated optical absorption spectrum of MA<sub>2</sub>Pb(SCN)<sub>2</sub>I<sub>2</sub>.

In conclusion, we have studied the photovoltaic properties of the 2D MA<sub>2</sub>Pb(SCN)<sub>2</sub>I<sub>2</sub> perovskite using the combination of materials synthesis, characterization and DFT calculations. We found that the 2D MA<sub>2</sub>Pb(SCN)<sub>2</sub>I<sub>2</sub> perovskite exhibits an indirect bandgap of 2.04 eV and a similar direct bandgap of 2.11 eV. The carriers are mobile, but are confined in the 2D layers. Our results indicate that, in contrast to previous literature reports, the 2D MA<sub>2</sub>Pb(SCN)<sub>2</sub>I<sub>2</sub> perovskite appears to be a less likely candidate for high-efficiency single-junction solar cell applications

due to its large bandgap and confined carriers in the 2D layers. However, it could perhaps still be considered for use as an absorber for the top cells of tandem solar cell applications if films are grown with the 2D layers aligned perpendicular to the substrates.

## EXPERIMENTAL SECTION

Synthesis of  $(\text{MA})_2\text{Pb}(\text{SCN})_2\text{I}_2$  powder: Stoichiometric amounts of  $\text{CH}_3\text{NH}_3\text{I}$  (Dyesol) and  $\text{Pb}(\text{SCN})_2$  (Aldrich) were carefully weighed and ground in a nitrogen-filled glovebox. The powdered mixture was then cold-pressed into a pellet in the glovebox, forming a dark purple pellet. The pellet was flame-sealed under vacuum ( $\sim 7 \times 10^{-7}$  Torr) in a quartz tube, which was cooled with liquid nitrogen to avoid the loss of volatile components. The reaction mixture was slowly heated to 100 °C over 1 hour, and kept at this temperature for 20 hours in a box furnace.

Synthesis of  $(\text{MA})_2\text{Pb}(\text{SCN})_2\text{I}_2$  thin film: First, the precursor solution was prepared by dissolving 0.323g  $\text{Pb}(\text{SCN})_2$  and 0.318g  $\text{CH}_3\text{NH}_3\text{I}$  in 1mL anhydrous N,N-dimethylformamide in a nitrogen-filled glovebox. Next, 50uL precursor solution was spin-coated onto a glass substrate at 4000 rpm, followed by quickly dropping 700uL diethyl ether onto the thin film, upon which the color of the film immediately changed from transparent to red. The obtained film was dried at room temperature for 20 minutes.

Characterization: X-ray diffraction measurements were performed on the obtained dark red product using a PANalytical Empyrean powder X-ray diffractometer (Cu  $K\alpha$  radiation) under ambient conditions and on the thin films using a Rigaku Ultima III (Cu  $K\alpha$  radiation) and with the operation conditions of 40 kV and 44 mA. An Enlitech QE-R Quantum Efficiency/Reflectivity measurement system (Enlitech) was used to carry out diffuse reflectance measurements. Absorbance spectra were measured by an ultraviolet–visible spectrophotometer

(PerkinElmer Lambda 1050). The calculation of the XRD patterns for MA<sub>2</sub>Pb(SCN)<sub>2</sub>I<sub>2</sub> was carried out using the Mercury 3.7 software.<sup>36</sup>

**DFT Calculations:** DFT calculations were performed for MA<sub>2</sub>Pb(SCN)<sub>2</sub>I<sub>2</sub> using the projector-augmented wave (PAW) method as implemented in the VASP code.<sup>37</sup> The plane wave cutoff energy was set to 500.0 eV. A  $\Gamma$ -centered 2×6×6 *k*-mesh was employed for sampling the Brillouin zone. For the exchange-correlation functionals, the PBE<sup>27</sup> functional without SOC and the HSE<sup>30,31</sup> hybrid functional with 43% of Hatree–Fock exchange and SOC, which reproduced the band the bandgap for MAPbI<sub>3</sub>,<sup>28,32,33</sup> were employed for MA<sub>2</sub>Pb(SCN)<sub>2</sub>I<sub>2</sub>. Prior to the electronic structure calculations, the structure was fully relaxed and considered to be converged when the total force on each atom was less than 0.01 eV Å<sup>-1</sup>.

## ASSOCIATED CONTENT

### **Supporting Information.**

The Supporting Information is available free of charge on the ACS Publications website at DOI. Calculated XRD pattern of MA<sub>2</sub>Pb(SCN)<sub>2</sub>I<sub>2</sub> (Figure S1), photos of MA<sub>2</sub>Pb(SCN)<sub>2</sub>I<sub>2</sub> powders and thin film (Figure S2), literature diffuse reflectance spectra (Figure S3).

## AUTHOR INFORMATION

### **Notes**

The authors declare no competing financial interests.

## ACKNOWLEDGMENT

This work was funded in part by the Office of Energy Efficiency and Renewable Energy (EERE), U.S. Department of Energy, under Award Number DE-EE0006712 and the Ohio

Research Scholar Program. BS acknowledges support from a Department of Energy (DOE) Office of Energy Efficiency and Renewable Energy (EERE) Postdoctoral Research Award administered by the Oak Ridge Institute for Science and Education (ORISE) for the DOE. ORISE is managed by Oak Ridge Associated Universities (ORAU) under DOE contract number DE-AC05-06OR23100. This research used the resources of the Ohio Supercomputer Center and the National Energy Research Scientific Computing Center, which is supported by the Office of Science of the U.S. Department of Energy under Contract No. DE-AC02-05CH11231.

## REFERENCES

- (1) Kojima, A.; Teshima, K.; Shirai, Y.; Miyasaka, T. Organometal Halide Perovskites as Visible-Light Sensitizers for Photovoltaic Cells. *J. Am. Chem. Soc.* **2009**, *131* (17), 6050–6051.
- (2) Sun, S.; Salim, T.; Mathews, N.; Duchamp, M.; Boothroyd, C.; Xing, G.; Sum, T. C.; Lam, Y. M. The Origin of High Efficiency in Low-Temperature Solution-Processable Bilayer Organometal Halide Hybrid Solar Cells. *Energy Environ. Sci.* **2014**, *7* (1), 399–407.
- (3) Xing, G.; Mathews, N.; Sun, S.; Lim, S. S.; Lam, Y. M.; Gratzel, M.; Mhaisalkar, S.; Sum, T. C. Long-Range Balanced Electron- and Hole-Transport Lengths in Organic-Inorganic  $\text{CH}_3\text{NH}_3\text{PbI}_3$ . *Science* **2013**, *342* (6156), 344–347.
- (4) Frost, J. M.; Butler, K. T.; Brivio, F.; Hendon, C. H.; van Schilfhaarde, M.; Walsh, A. Atomistic Origins of High-Performance in Hybrid Halide Perovskite Solar Cells. *Nano Lett.* **2014**, *14* (5), 2584–2590.

- (5) Niu, G.; Li, W.; Meng, F.; Wang, L.; Dong, H.; Qiu, Y. Study on the Stability of  $\text{CH}_3\text{NH}_3\text{PbI}_3$  Films and the Effect of Post-Modification by Aluminum Oxide in All-Solid-State Hybrid Solar Cells. *J. Mater. Chem. A* **2014**, 2 (3), 705–710.
- (6) Han, Y.; Meyer, S.; Dkhissi, Y.; Weber, K.; Pringle, J. M.; Bach, U.; Spiccia, L.; Cheng, Y.-B. Degradation Observations of Encapsulated Planar  $\text{CH}_3\text{NH}_3\text{PbI}_3$  Perovskite Solar Cells at High Temperatures and Humidity. *J. Mater. Chem. A* **2015**, 3 (15), 8139–8147.
- (7) Habisreutinger, S. N.; Leijtens, T.; Eperon, G. E.; Stranks, S. D.; Nicholas, R. J.; Snaith, H. J. Carbon Nanotube/Polymer Composites as a Highly Stable Hole Collection Layer in Perovskite Solar Cells. *Nano Lett.* **2014**, 14 (10), 5561–5568.
- (8) Smith, I. C.; Hoke, E. T.; Solis-Ibarra, D.; McGehee, M. D.; Karunadasa, H. I. A Layered Hybrid Perovskite Solar-Cell Absorber with Enhanced Moisture Stability. *Angew. Chemie* **2014**, 126 (42), 11414–11417.
- (9) Yang, S.; Wang, Y.; Liu, P.; Cheng, Y.-B.; Zhao, H. J.; Yang, H. G. Functionalization of Perovskite Thin Films with Moisture-Tolerant Molecules. *Nat. Energy* **2016**, No. January, 15016.
- (10) Mei, A.; Li, X.; Liu, L.; Ku, Z.; Liu, T.; Rong, Y.; Xu, M.; Hu, M.; Chen, J.; Yang, Y.; et al. A Hole-Conductor-free, Fully Printable Mesoscopic Perovskite Solar Cell with High Stability. *Sci.* **2014**, 345 (6194), 295–298.
- (11) Jiang, Q.; Rebollar, D.; Gong, J.; Piacentino, E. L.; Zheng, C.; Xu, T. Pseudohalide-Induced Moisture Tolerance in Perovskite  $\text{CH}_3\text{NH}_3\text{Pb}(\text{SCN})_2\text{I}$  Thin Films. *Angew. Chemie* **2015**, 127 (26), 7727–7730.

- (12) Chen, Y.; Li, B.; Huang, W.; Gao, D.; Liang, Z. Efficient and Reproducible CH<sub>3</sub>NH<sub>3</sub>PbI<sub>3-x</sub>(SCN)<sub>x</sub> Perovskite Based Planar Solar Cells. *Chem. Commun.* **2015**, 51 (60), 11997–11999.
- (13) Daub, M.; Hillebrecht, H. Synthesis, Single-Crystal Structure and Characterization of (CH<sub>3</sub>NH<sub>3</sub>)<sub>2</sub>Pb(SCN)<sub>2</sub>I<sub>2</sub>. *Angew. Chemie Int. Ed.* **2015**, 54 (38), 11016–11017.
- (14) Ganose, A. M.; Savory, C. N.; Scanlon, D. O. (CH<sub>3</sub>NH<sub>3</sub>)<sub>2</sub>Pb(SCN)<sub>2</sub>I<sub>2</sub>: A New More Stable Structural Motif for Hybrid Halide Photovoltaics? *J. Phys. Chem. Lett.* **2015**, 4594–4598.
- (15) Umebayashi, T.; Asai, K.; Kondo, T.; Nakao, A. Electronic Structures of Lead Iodide Based Low-Dimensional Crystals. *Phys. Rev. B* **2003**, 67 (15), 155405.
- (16) Saparov, B.; Hong, F.; Sun, J.-P.; Duan, H.-S.; Meng, W.; Cameron, S.; Hill, I. G.; Yan, Y.; Mitzi, D. B. Thin-Film Preparation and Characterization of Cs<sub>3</sub>Sb<sub>2</sub>I<sub>9</sub>: A Lead-Free Layered Perovskite Semiconductor. *Chem. Mater.* **2015**, 27 (16), 5622–5632.
- (17) Liao, M.; Xiao, Z.; Ran, F.-Y.; Kumomi, H.; Kamiya, T.; Hosono, H. Effects of Pb Doping on Hole Transport Properties and Thin-Film Transistor Characteristics of SnO Thin Films. *ECS J. Solid State Sci. Technol.* **2015**, 4 (3), Q26–Q30.
- (18) Ran, F.-Y.; Xiao, Z.; Toda, Y.; Hiramatsu, H.; Hosono, H.; Kamiya, T. N-Type Conversion of SnS by Isovalent Ion Substitution: Geometrical Doping as a New Doping Route. *Sci. Rep.* **2015**, 5, 10428.
- (19) Ueda, K.; Inoue, S.; Hosono, H.; Sarukura, N.; Hirano, M. Room-Temperature Excitons in Wide-Gap Layered-Oxysulfide Semiconductor: LaCuOS. *Appl. Phys. Lett.* **2001**, 78 (16),

2333.

- (20) Ueda, K.; Hiramatsu, H.; Ohta, H.; Hirano, M.; Kamiya, T.; Hosono, H. Single-Atomic-Layered Quantum Wells Built in Wide-Gap Semiconductors  $\text{LnCuOCh}$  (Ln=lanthanide, Ch=chalcogen). *Phys. Rev. B* **2004**, *69* (15), 155305.
- (21) Frey, G. L.; Elani, S.; Homyonfer, M.; Feldman, Y.; Tenne, R. Optical-Absorption Spectra of Inorganic Fullerenelike  $\text{MS}_2$  (M = Mo, W). *Phys. Rev. B* **1998**, *57* (11), 6666–6671.
- (22) Mak, K. F.; Lee, C.; Hone, J.; Shan, J.; Heinz, T. F. Atomically Thin  $\text{MoS}_2$ : A New Direct-Gap Semiconductor. *Phys. Rev. Lett.* **2010**, *105* (13), 136805.
- (23) Sandroff, C. J.; Hwang, D. M.; Chung, W. M. Carrier Confinement and Special Crystallite Dimensions in Layered Semiconductor Colloids. *Phys. Rev. B* **1986**, *33* (8), 5953.
- (24) Boldish, S. I.; White, W. B. Optical Band Gaps of Selected Ternary Sulfide Minerals. *Am. Mineral.* **1998**, *83* (7-8), 865–871.
- (25) Eckhardt, H.; Chance, R. R. Defect States in Polyacetylene: A Photoacoustic and Diffuse Reflectance Study. *J. Chem. Phys.* **1983**, *79* (11), 5698.
- (26) Qiu, J.; Qiu, Y.; Yan, K.; Zhong, M.; Mu, C.; Yan, H.; Yang, S. All-Solid-State Hybrid Solar Cells Based on a New Organometal Halide Perovskite Sensitizer and One-Dimensional  $\text{TiO}_2$  Nanowire Arrays. *Nanoscale* **2013**, *5* (8), 3245.
- (27) Perdew, J. P.; Burke, K.; Ernzerhof, M. Generalized Gradient Approximation Made Simple. *Physical Review Letters*. 1996, pp 3865–3868.

- (28) Mosconi, E.; Amat, A.; Nazeeruddin, M. K.; Grätzel, M.; De Angelis, F. First-Principles Modeling of Mixed Halide Organometal Perovskites for Photovoltaic Applications. *J. Phys. Chem. C* **2013**, *117* (27), 13902–13913.
- (29) Even, J.; Pedesseau, L.; Jancu, J.-M.; Katan, C. Importance of Spin–Orbit Coupling in Hybrid Organic/Inorganic Perovskites for Photovoltaic Applications. *J. Phys. Chem. Lett.* **2013**, *4* (17), 2999–3005.
- (30) Heyd, J.; Scuseria, G. E.; Ernzerhof, M. Hybrid Functionals Based on a Screened Coulomb Potential. *J. Chem. Phys.* **2003**, *118* (18), 8207–8215.
- (31) Heyd, J.; Scuseria, G. E.; Ernzerhof, M. Erratum: “Hybrid Functionals Based on a Screened Coulomb Potential” [J. Chem. Phys. 118, 8207 (2003)]. *J. Chem. Phys.* **2006**, *124* (21), 219906.
- (32) Du, M. H. Efficient Carrier Transport in Halide Perovskites: Theoretical Perspectives. *J. Mater. Chem. A* **2014**, *2* (24), 9091.
- (33) Du, M.-H. Density Functional Calculations of Native Defects in CH<sub>3</sub>NH<sub>3</sub>PbI<sub>3</sub>: Effects of Spin–Orbit Coupling and Self-Interaction Error. *J. Phys. Chem. Lett.* **2015**, *6* (8), 1461–1466.
- (34) Aroyo, M. I.; Orobengoa, D.; de la Flor, G.; Tasci, E. S.; Perez-Mato, J. M.; Wondratschek, H. Brillouin-Zone Database on the Bilbao Crystallographic Server. *Acta Crystallogr.* **2014**, *A70* (2), 126–137.
- (35) Zhou, Y.; Wang, L.; Chen, S.; Qin, S.; Liu, X.; Chen, J.; Xue, D.-J.; Luo, M.; Cao, Y.;

- Cheng, Y.; et al. Thin-Film Sb<sub>2</sub>Se<sub>3</sub> Photovoltaics with Oriented One-Dimensional Ribbons and Benign Grain Boundaries. *Nat. Photonics* **2015**, *9* (6), 409–415.
- (36) Macrae, C. F.; Bruno, I. J.; Chisholm, J. A.; Edgington, P. R.; McCabe, P.; Pidcock, E.; Rodriguez-Monge, L.; Taylor, R.; van de Streek, J.; Wood, P. A. Mercury CSD 2.0 – New Features for the Visualization and Investigation of Crystal Structures. *J. Appl. Crystallogr.* **2008**, *41* (2), 466–470.
- (37) Kresse, G.; Furthmüller, J. Efficient Iterative Schemes for Ab Initio Total-Energy Calculations Using a Plane-Wave Basis Set. *Physical Review B*. **1996**, *54* (16), 11169–11186.